Int. J. Electrochem. Sci., 15 **(2020)** 11584 – 11593, doi: 10.20964/2020.11.26

International Journal of
ELECTROCHEMICAL
SCIENCE
www.electrochemsci.org

Microstructure and Corrosion Resistance of Fe314 Alloy Prepared by Laser Cladding on EA4T Steel Surface

Yujiang Xie[1, 2], Bensheng Huang[1,], Jia Zhuang[1,*], Wenjing Chen[3], Jie Hu[1]*

[1] School of New Energy and Materials, Southwest Petroleum University, Chengdu, 610500, China
[2] School of Engineering, Southwest Petroleum University, Nanchong, 637001, China
[3] School of Materials Science and Engineering, Xihua University, Chengdu, 610039, China
[*]E-mail: hbslxp@163.com; zhuangjia1001@126.com

Received: 26 July 2020 / *Accepted:* 27 August 2020 / *Published:* 30 September 2020

An Fe314 alloy cladding layer was prepared on EA4T steel by laser cladding. Scanning electron microscopy (SEM), X-ray diffraction (XRD), energy dispersive spectroscopy (EDS) and an electrochemical workstation were used to investigate the microstructure, phase composition, element distribution and corrosion resistance of the cladding layer. The results showed that the microstructure of the cladding layer is columnar crystal and equiaxial crystal, the interior of the cladding layer grains is mainly an austenite phase, and the intergranular precipitates mainly include Fe_3C, FeB and Cr_3C_2. The closer the cladding zone is to the bonding zone, the lower the Cr element content and the higher the Fe element content. Compared with the substrate, the cladding layer has excellent corrosion resistance.

Keywords: EA4T steel; laser cladding; microstructure; corrosion resistance

1. INTRODUCTION

Railway axles are the key bearing components of locomotive and rolling stock bogies, and damage to railway axles can directly lead to major vehicle accidents. During operation, train axles are subject to the combined actions of alternating loads and a corrosive environment, which can easily lead to damage [1-3]. EA4T steel is a low-carbon and low-alloy steel used for the hollow axles of high-speed trains. It has excellent mechanical properties but poor corrosion resistance in atmospheric environments, and its surface is prone to corrosion [4-7]. Therefore, improving the corrosion resistance of railway axle surfaces in atmospheric environments can effectively reduce the damage caused by surface corrosion.

Laser cladding, as an advanced surface processing technology, has the advantages of low substrate deformation and high interfacial bonding strength [8-10]. In addition, the laser cladding product has a low dilution rate and a good effect in terms of microstructure, hardness and porosity [11-13]. In the laser cladding process, a laser is used as the heat source to heat and melt the specific alloy powder

so that cladding, with special properties such as wear, corrosion and fatigue resistance, can be formed on the surface of the substrate, thus effectively extending the service life of the substrate material and increasing economic benefits [14-17].

Recently, many scholars have used laser cladding processes to improve the corrosion resistance of material surfaces, and good results have been obtained. J.L. Chen et al. [18] prepared an Fe-based alloy coating on the surface of 35CrMo steel by a laser cladding process and studied the microstructure and corrosion resistance of the coating. The results showed that the corrosion resistance of the metal surface was significantly improved by the coating. G. Li et al. [19] used laser cladding technology and ultrasonic plasma spraying to prepare Fe-based amorphous coatings on the surface of a 45 steel substrate. The microstructure and properties of the two coatings were compared, and the results showed that the laser cladding has higher uniform corrosion resistance and better friction and wear performance than the plasma spraying coating. X.W. Qiu et al. [20] prepared a Ni60B alloy laser cladding on the surface of 40Cr steel. The microstructure and properties of the cladding were studied. The results showed that the hardness and corrosion resistance of the substrate surface were improved by the laser cladding.

In this paper, Fe314 alloy cladding is prepared on the surface of EA4T steel by a laser cladding process with optimized parameters. The microstructure and corrosion resistance of the cladding are studied to provide a theoretical basis for reducing corrosion damage to EA4T railway axle steel during use.

2. EXPERIMENT

2.1. Materials and methods

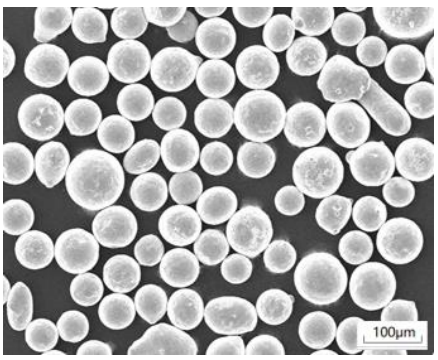

Figure 1. Morphology of Fe314 alloy powder

Table 1 Chemical composition of EA4T steel and Fe314 alloy powder (wt. %)

Materials	C	Cr	Si	Ni	B	Mn	Mo	Cu	S	P	Fe
EA4T	0.26	1.04	0.34	0.26	–	0.74	0.25	0.15	0.002	0.008	Others
Fe314	0.1	17.5	0.12	10.5	0.65	–	–	–	–	–	Others

EA4T railway axle steel with a size of 110 mm×100 mm×10 mm was used as the substrate in the experiment. The substrate was polished with sandpaper to remove the oxide layer on the surface, and the metal surface was cleaned with acetone and anhydrous ethanol. The cladding material is Fe314 spherical

alloy powder with a particle size of approximately 55~115 μm, and its morphology is shown in Figure 1. The chemical compositions of the EA4T steel and Fe314 alloy powder are shown in Table 1.

A Dista-3000 semiconductor laser was used for the laser cladding test. In combination with an FHPH-20-type carrier gas powder feeder, laser cladding was carried out in a side-by-side synchronous mode. During the laser cladding process, argon was used as a protective gas to protect the molten pool. The laser cladding parameters are shown in Table 2.

Table 2 Laser cladding parameters

Laser power/W	Scanning rate/(mm/min)	Spot diameter/mm	Flow rate of powder feeding gas (L/min)	Powder feeding voltage (V)	Shield gas flow (L/min)	Overlap rate/%
1800	280	5	5	13	22	50

The laser cladding samples were cut in a direction perpendicular to the laser scanning, and the cladding samples were corroded with aqua regia. A Tescan Vega 3 scanning electron microscope (SEM) was used to observe the microstructure of the cladding. Chemical composition analysis of the cladding was carried out by Oxford AZtec X-MAX20 energy dispersive spectroscopy (EDS). The laser cladding phase structures were analyzed by DX-2700B X-ray diffraction (XRD). The scanning angle of 2θ was 10° ~ 90°, and the scanning speed was 0.05°/s.

The electrochemical impedance spectroscopy (EIS) and polarization curves of the Fe314 alloy laser cladding were measured by a Gamry Reference 3000 electrochemical workstation with a 3.5% NaCl solution as the corrosion solution at room temperature. A three-electrode system was used in the test: the test sample was the working electrode, the reference electrode (RE) was the saturated calomel electrode, and the auxiliary electrode (CE) was the platinum electrode. The corrosion area of the cladding in the NaCl solution was 0.8 cm^2. Before the test, the sample was immersed in NaCl solution for 0.5 hours to ensure that the solution reached a stable state before each test. The scanning rate of the polarization test was 0.1 $mV \cdot s^{-1}$, the open circuit potential (OCP) was -1.8 V, and the potential range was -1.7 V ~ -1.3 V. EIS tests were performed at frequencies ranging from 100 kHz to 0.01 Hz. The corrosion rate of the cladding was obtained by using the Tafel extrapolation method, and the experimental EIS data were fitted by using ZSimDemo software to study the corrosion resistance of the cladding.

3. RESULTS AND DISCUSSION

3.1 The microstructure of the Fe314 alloy laser cladding

The microstructures of the Fe314 alloy laser cladding cross-sections are shown in Figure 2. Figure 2(a) shows an obvious bonding area between the cladding layer and the substrate, which means that metallurgical bonding occurred between the Fe314 alloy laser cladding and the EA4T substrate. No cracks were found in the cladding layer, bonding zone or substrate. Large columnar crystals were formed

at the bottom of the cladding layer, and equiaxial crystals were dominant in the middle and top of the cladding layer. The equiaxed grains at the top were larger than those in the middle of the cladding layer.

The substrate has a strong heat transfer effect at a low temperature, resulting in a substantial degree of undercooling temperature at the bottom of the cladding pool. In addition, the surface of the substrate can be used as a substrate for nonuniform nucleation. Liquid metal nucleates at the interface between the molten pool and the substrate at first and grows epitaxially along the direction opposite the direction with the greatest heat loss [21]. However, grains growing in other directions are restricted by the surrounding grains, forming coarse columnar grains growing in the direction opposite of the heat dissipation, as shown in Figure 2 (d).

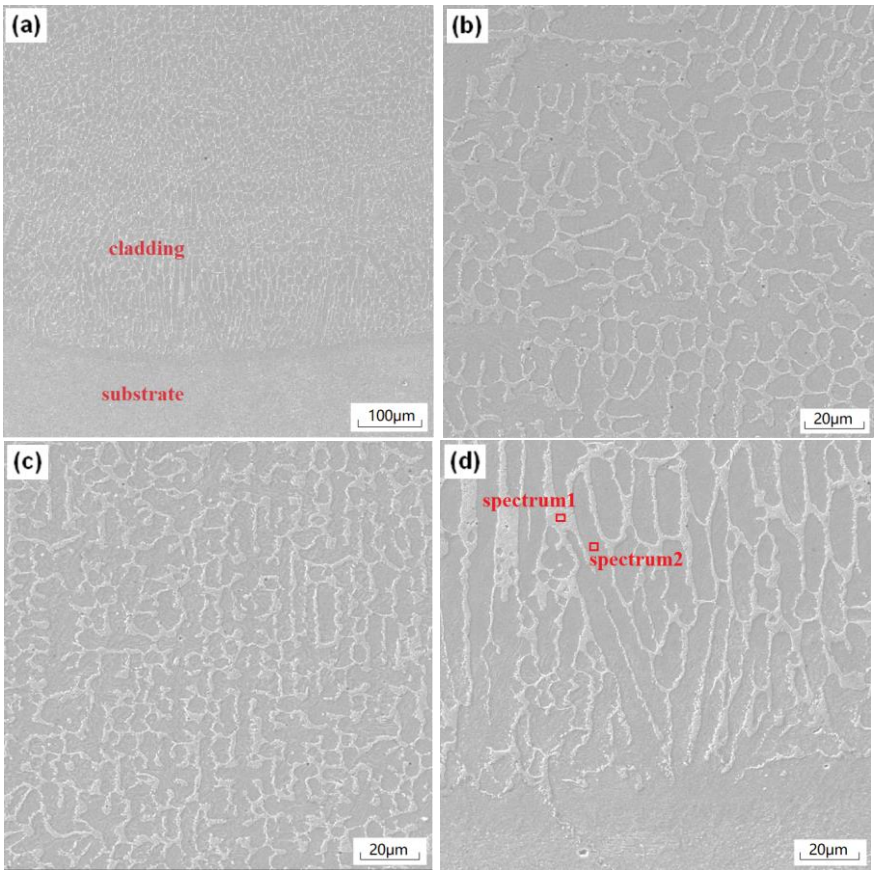

Figure 2. Cross-section morphology of the Fe314 alloy laser cladding: (a) the complete cladding; (b) the top of the cladding layer; (c) the middle of the cladding layer; (d) the bottom of the cladding layer

The substrate was heated with the growth of columnar crystals, the cooling capacity of the substrate to the molten pool was reduced, and the heat dissipation gradually became disoriented. In addition, complex chemical reactions among various elements in the liquid metals resulted in the formation of some intermetallic compounds, which provided the conditions for the formation of crystal nuclei. Thus, equiaxed crystals are formed, as shown in Figure 2 (b) and Figure 2 (c). As the cladding layer is formed by a multilayer and multipass laser cladding process, the latter cladding layer will play

the role of heat treatment for the former one, which is equivalent to a normalizing treatment, so that the structures of the former cladding layer are relatively small, as shown in Figure 2 (c). Because the top of the cladding layer is the last cladding layer, there is no heat treatment effect on it by subsequent cladding; therefore, the structures are relatively large, as shown in Figure 2 (b).

3.2 Phase composition and element distribution

Figure 3 shows the XRD pattern of the Fe314 alloy cladding layer. The figure shows that the phases in the cladding layer are mainly austenite, and there are also Fe_3C, FeB and $Cr3C_2$ phases. Based on the analysis in Figure 2, it can be seen that the gray grain is mainly the austenite phase, while the white intergranular precipitates mainly contain Fe_3C, FeB and Cr_3C_2. As shown in Figure 2 (d), the grains and intergranular precipitates were analyzed by EDS, and the results are shown in Figure 4 and Table 3. The EDS analysis results show that the Cr content in the grains was significantly lower than that of the white intergranular precipitates, while the Fe content in the grains was significantly higher than that of the white intergranular precipitates. Combined with the XRD results, it can be seen that carbide Cr_3C_2 is formed between the crystals, making the Cr content higher than that inside the grains.

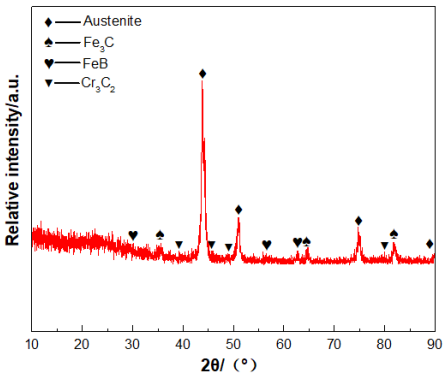

Figure 3. XRD phase analysis of the Fe314 alloy laser cladding

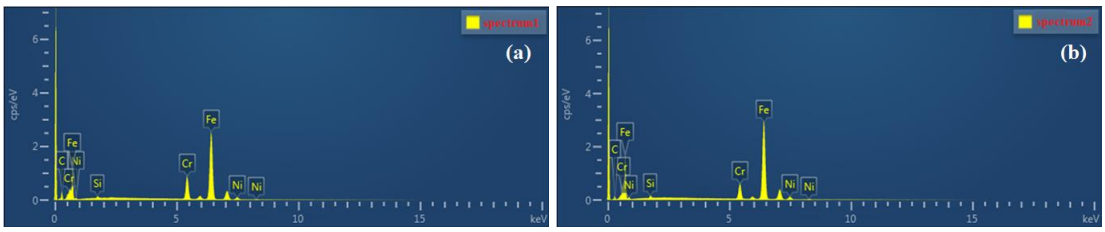

Figure 4. EDS analysis of the Fe314 alloy laser cladding: (a) energy spectrum of intergranular precipitates; (b) energy spectrum inside the grains

Table 3. Element distribution inside the grains and intergranular precipitates (wt.%)

Elements	C	Si	Cr	Fe	Ni
spectrum1	0.26	0.49	16.01	79.14	4.10
spectrum2	0.10	0.67	9.69	84.63	4.91

EDS line scanning was carried out on the cross-section of the sample from the surface of the cladding layer to the substrate, and the results are shown in Figure 5. Generally, all elements in the cladding layer are evenly distributed. Fe and Cr show a relatively obvious wave peak, which is caused by the large difference in the content of these two elements in and between grains. The Cr content decreases and the Fe content increases as the scan moves closer to the substrate. The Cr content in the bonding area between the cladding layer and the substrate decreased significantly because the substrate had a dilution effect on the cladding layer, and the closer the cladding layer was to the bonding area, the more obvious the dilution effect was, and the dilution rate gradually increased.

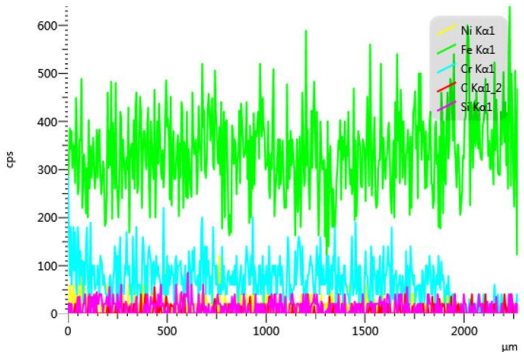

Figure 5. EDS line scanning of the cladding layer

3.3 The corrosion resistance of the Fe314 alloy laser cladding

Figure 6 shows the Nyquist plots and Bode plots of the EA4T steel substrate and Fe314 alloy cladding layer in a 3.5% NaCl solution. Figure 6 (a) indicates that the Nyquist plots of the EA4T steel substrate show only one capacitive reactance arc, while the Fe314 alloy cladding layer shows two capacitive reactance arcs. Moreover, the cladding layer has a larger arc radius than that of the substrate, indicating that the cladding layer has better corrosion resistance. Figure 6 (b) shows that the impedance value of the Fe314 alloy cladding layer is significantly higher than that of the EA4T steel substrate. This indicates that the penetration degree of the solution into the cladding layer is less than that of the substrate, and the electrochemical corrosion resistance of the cladding layer is better than that of the substrate [22-23]. Figure 6 (c) shows a constant phase diagram of the EA4T substrate and Fe314 alloy cladding layer. The figure shows that the substrate has only one constant phase element, while the cladding layer has two constant phase elements, which further indicates that the cladding layer is a bilayer structure composed of itself and its surface film layer. This corresponds to the two capacitive reactance arcs of the cladding layer in the Nyquist plots. To prove the validity of this detection result, ZSimDemo software was used to fit the EIS experimental data. After analysis, two equivalent circuit

diagrams, as shown in Figure 7, were used to fit the EIS data of the substrate and cladding layer [24]. In these two equivalent circuits, Rs is the resistance of the solution between the sample and the reference electrode. R1 is the resistance of the surface film layer of the cladding layer, and R2 is the internal resistance of the cladding layer. CPE1 is a constant phase element on the surface of the cladding layer, and CPE2 is a constant phase element inside the cladding layer. The fitting results of these two equivalent circuit diagrams are shown in Table 4 and Table 5. By comparing the data in the tables, it can be seen that the corrosion resistance of the cladding layer with the double-layer structure is better than that of the substrate. The data in Table 5 show that n1 is larger and closer to 1 than n2, R1 is larger than R2, and CPE1 is smaller than CPE2. The corrosion resistance of the material increases with increasing n value and R value and decreases with increasing CPE value. Therefore, it can be inferred that the surface film layer of the cladding layer has better corrosion resistance than the cladding layer itself [25-26]. Referring to Table 1, it can be seen that the Fe314 alloy powder contains a large amount of Cr. After the Fe314 alloy cladding layer is prepared by the laser cladding process, the abundant Cr element in the cladding layer interacts with oxygen in the air to form a dense Cr_2O_3 oxide film on the surface of the cladding layer. The Cr_2O_3 oxide film can effectively isolate the cladding layer from the air medium, thus delaying the corrosion of the cladding layer. The cladding layer itself can also play a role in isolation protection for the substrate. Therefore, the oxide film on the surface of the cladding layer and the cladding layer itself provide double isolation protection for the substrate, effectively preventing it from being corroded [27-28].

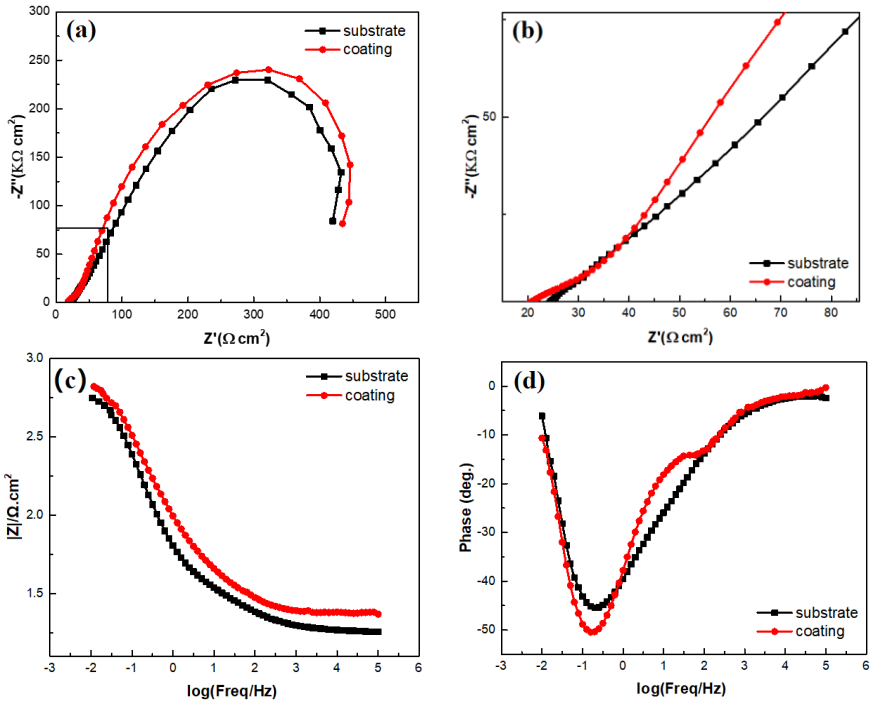

Figure 6. EIS spectra of the EA4T substrate and Fe314 alloy cladding in 3.5wt.% NaCl solution: (a) Nyquist plots; (b) local enlarged view of (a); (c, d) Bode plots

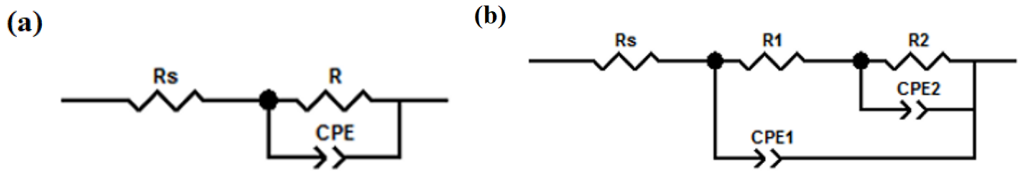

Figure 7. Equivalent circuits of the EA4T substrate and Fe314 alloy cladding in 3.5wt.% NaCl solution: (a) EA4T substrate; (b) Fe314 alloy cladding

Table 4. Electrochemical parameters obtained from EIS spectra of the EA4T substrate in 3.5wt.% NaCl solution

Sample	Rs (Ω.cm2)	CPE ($Ω^{-1}·cm^{-2}Sn$)	n	R ($Ω.cm^2$)
EA4T substrate	7.95	$3.593×10^{-3}$	0.5821	$1.012×10^{+3}$

Table 5. Electrochemical parameters obtained from EIS spectra of Fe314 alloy cladding in 3.5wt.% NaCl solution

Sample	Rs ($Ω.cm^2$)	CPE1 ($Ω^{-1}·cm^{-2}S^n$)	n1	R_1 ($Ω.cm^2$)	CPE2 ($Ω^{-1}·cm^{-2}$ S^n)	n2	R_2 ($Ω.cm^2$)
cladding	8.42	$1.661×10^{-3}$	0.8536	$5.995×10^{+3}$	$3.74×10^{-3}$	0.6598	$2.701×10^{+1}$

Figure 8 shows the potentiodynamic polarization curves of the EA4T steel substrate and Fe314 alloy cladding layer. The self-corrosion potential (Ecorr), self-corrosion current (icorr) and corrosion rate (Rcorr) of the substrate and the cladding were obtained by Tafel extrapolation, as shown in Table 6. As seen from the data in Table 6, compared with the matrix, the cladding layer has a higher self-etching potential, a smaller self-etching current and a slower corrosion rate. The corrosion resistance of the cladding layer is better than that of the substrate. An analysis of the dynamic potential polarization curves of the EA4T steel substrate and Fe314 alloy cladding shows that the Fe314 alloy cladding has better corrosion resistance than the EA4T steel substrate, and the cladding layer can effectively protect the substrate in a corrosive environment.

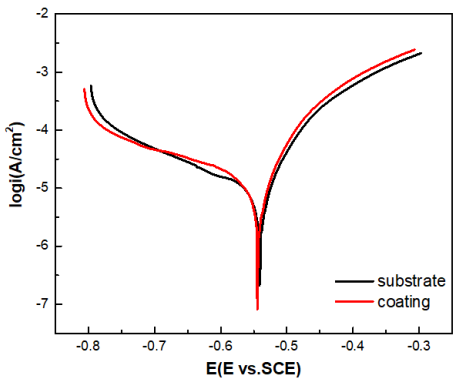

Figure 8. Polarization curves of the EA4T substrate and Fe314 alloy cladding in 3.5wt.% NaCl solution

Table 6. Electrochemical data from the polarization tests for the EA4T substrate and Fe314 alloy cladding in 3.5wt.% NaCl solution

Sample	Ecorr/V	Icorr/(A/cm2)	Corrosion rate/(mm/a)
Substrate	-0.544	3.21×10^{-5}	4.674×10^{-1}
coating	-0.541	1.02×10^{-5}	1.469×10^{-1}

4. CONCLUSIONS

(1) The Fe314 alloy cladding prepared on a EA4T steel substrate by a laser cladding process formed a good metallurgical combination with the substrate. Coarse columnar crystals were formed at the bottom of the cladding layer, the middle and top of the cladding layer were dominated by equiaxial crystals, and the grains at the top of the cladding layer were larger than those in the middle.

(2) The microstructures of the cladding layer are mainly composed of grains and intergranular precipitates. The grains mainly contain an austenite phase, and the intergranular precipitate phase mainly contains Fe_3C, FeB and Cr_3C_2 phases. The distribution of all elements in the cladding layer is relatively uniform. However, due to the dilution effect of the matrix, Cr content decreases and Fe content increases in the cladding zone closer to the interface.

(3) Only one capacitive reactance arc occurred in the Nyquist plots of the EA4T steel substrate, while two capacitive reactance arcs occurred in the Fe314 alloy cladding layers. The radius of the capacitive reactance arc of the cladding layer is larger than that of the EA4T steel substrate. Compared with the substrate, the self-corrosion potential is higher, the self-corrosion current is smaller, and the corrosion rate is slower in the cladding layer. The corrosion rates of the substrate and cladding layer are 4.674×10^{-1}mm/a and 1.469×10^{-1}mm/a, respectively. The Fe314 alloy laser cladding has better corrosion resistance than the EA4T steel substrate and can effectively protect the substrate in a corrosive environment.

ACKNOWLEDGEMENT
The study was supported by a grant from the fund of the science and technology strategic cooperation project of city and university of Nanchong city (Grant No. 18SXHZ0037.)

DECLARATION OF INTEREST
The authors declare that there are no conflicts of interest regarding the publication of this paper.

References

1. U. Zerbst, S. Beretta, G. KöHler, G. Koehler, A. Lawton, M. Vormwald, H. Th. Beier, C. Klinger, I. Cerny, J. Rudlin, T. Heckel, D. Klingbeil, *Eng. Fract. Mech.*, 98 (2013) 214.
2. S. Beretta, F. Sangalli, J. Syeda, D. Panggabean, J. Rudlin, RAAI Project: Life-prediction and prognostics for railway axles under corrosion-fatigue damage, ESIS-Technical-Committee 24

Workshop on Integrity of Railway Structures, Leoben, AUSTRIA, 2016, 64-70.
3. S. Beretta, A. Lo Conte, J. Rudlin, D. Panggabean, *Eng. Fail. Anal.*, 47 (2015) 252.
4. W.J. Chen, H. Chen, C.C. Li, X.L. Wang, Q. Cai, *Eng. Fail. Anal.*, 79 (2017) 120.
5. Z.W. Xu, S.C. Wu, X.S. Wang, *Int. J. Fatigue*, 123 (2019) 79.
6. S.C. Wu, Z.W. Xu, G.Z. Kang, W.F. He, *Int. J. Fatigue*, 117 (2018) 90.
7. P. Pokorny, T. Vojtek, L. Náhlík, P. Hutar, *Eng. Fract. Mech.*, 185 (2017) 2.
8. M.M. Quazi, M.A. Fazal, A.S.M.A. Haseeb, Farazila Yusof, H. H. Masjuki, A. Arslan, *Lasers Manuf. Mater. Process.*, 3 (2016) 1.
9. W.J. Chen, H. Chen, Y.J. Wang, C.C. Li, X.L. Wang, *Int. J. Mod. Phys. B*, 31 (2017) 16.
10. X. Su, W. Tao, Y.B. Chen, X. Chen, Z. Tian, *Mater. Lett.*, 195 (2017) 228.
11. Akio HIROSE, Kojiro F. KOBAYASHI, *ISIJ Int.*, 35 (1995) 757.
12. N.A. HELLA, *Opt. Eng.*, 17 (1978) 198.
13. L. Dubourg, D. Ursescu, F. Hlawka, A. Cornetb, *Wear*, 258 (2005) 1745.
14. X.X. Duan, S.Y. Gao, Q. Dong, Y.F. Zhou, M.Z. Xi, X.P. Xian, B. Wang, *Surf. Coat. Technol.*, 291 (2016) 230.
15. X.T. Feng, J.B. Lei, H. Gu, S.F. Zhou, *Chin. Phys. B*, 28 (2019) 383.
16. H.X. Liu, C.Q. Wang, X.W. Zhang, Y.H. Jiang, C.X. Cai, S.J. Tang, *Surf. Coat. Technol.*, 228 (2013) S296.
17. X. Tong, F.H. Li, M. Liu, M.J. Dai, H. Zhou, *Opt. Laser Technol.*, 42 (2010) 1154.
18. J.L. Chen, Y.J. Zhou, C. Shi, D.H. Mao, *Metals*, 7 (2017) 435.
19. G. Li, Y.Y. Gan, C.H. Liu, Y. Shi, Y.C. Zhao, S.Z. Kou, *Coatings*, 10 (2020) 73.
20. X.W. Qiu, G. Li, X. Ren, L. Qiu, *Rare Metal Mat. Eng.*, 38 (2009) 325.
21. Y.C. Zhang, Z.G. Li, P.L. Nie, Y.X. Wu, *Metall. Mater. Trans. A-Phys. Metall. Mater. Sci.*, 44A (2013) 708.
22. H. Zhang, Y. Zou, Z.D. Zou, D.T. Wu, *J. Alloy. Compd.*, 622 (2015) 62.
23. J. Hu, P. Wang, D.D. Liao, X.Y. Sun, Z.Y. Gong, J.W. Liu, D. Xiong, D. Xiang, X.T. Zu, X.W. Wei, *Int. J. Electrochem. Sci.*, 15 (2020) 4978.
24. M.Q. Tang, J.F. Wang, Z.Q. Feng, G. Li, Z.W. Yan, R.Z. Zhang, *Ceram. Int.*, 45 (2019) 16918.
25. P. Wang, W.J. Cao, B. Yang, Q.G. Yang, J. Pu, Z.Y. Gong, J. Hu, X.Y. Guo, D. Xiang. *Int. J. Appl. Ceram. Technol.*, 16 (2019) 2273.
26. W.Y. Liu, Y. Liu, Y.H. Lin, Z. Zhang, S.B. Feng, M. Talha, Y.S. Shi, T.H. Shi, *Appl. Surf. Sci.*, 475 (2019) 645.
27. H.J. Lee, H.W. Lee, *Int. J. Electrochem. Sci.*, 10 (2015) 8028.
28. H.Y. Li, S.W. Zou, C.F. Dong, K. Xiao, X.G. Li, P. Zhong, *Int. J. Electrochem. Sci.*, 12 (2017) 529.